Optics Letters

Nonlinearity-aware optoelectronic terahertz discrete multitone signal transmission with a zero-bias diode

Lu Zhang,[1,2] Mengyao Qiao,[1] Shiwei Wang,[1] Zijie Lu,[1] Le Zhang,[3] Xiaodan Pang,[4] Xianmin Zhang,[1] and Xianbin Yu[1,2,*]

[1]The College of Information Science and Electronic Engineering, Zhejiang University, Hangzhou 310027, China
[2]Zhejiang Lab, Hangzhou 311121, China
[3]China Jiliang University, Hangzhou 310018, China
[4]Royal Institute of Technology, Stockholm SE-10044, Sweden
*Corresponding author: xyu@zhejianglab.com

Received 8 July 2020; revised 3 August 2020; accepted 3 August 2020; posted 4 August 2020 (Doc. ID 401414); published 4 September 2020

The terahertz band has been recognized as a promising candidate to support future rate-greedy applications such as 6G communications. Optoelectronic terahertz communications are beneficial for the realization of high-speed transmission. In this Letter, we propose and experimentally demonstrate an optoelectronic terahertz transmission system with intensity modulation and direct detection, where a discrete multitone (DMT) waveform with high-order quadrature amplitude modulation (QAM) is used. A zero-bias diode (ZBD) is used in the system as a simple, cost-effective direct detection terahertz receiver. A nonlinearity-aware digital signal reception routine is proposed to mitigate the nonlinear impairments induced by subcarrier-to-subcarrier beating interference from the ZBD. In this experiment, up to a 60 Gbit/s line rate 16QAM-DMT signal is successfully transmitted over a 3 m wireless link in the 310 GHz band, and the mean signal-to-noise ratio is improved by 3 dB with nonlinearity-aware signal processing routine. The advantageous features of such a scheme make it a promising solution for terahertz wireless communications.

https://doi.org/10.1364/OL.401414

To cope with the ever-increasing capacity demand from rate-greedy applications, the terahertz (0.3–10 THz) band technologies that make use of the rich spectrum resources are widely analyzed for future 6G communications [1–4]. The mechanisms of terahertz wireless communication systems are mainly categorized as pure-electronic schemes and optoelectronic schemes. The pure-electronic schemes suffer from the impairments such as harmonic-tone distortions and bandwidth limitation. Comparatively, optoelectronic schemes provide benefits such as larger modulation bandwidth, and its photomixing mechanism ensures high signal transparency to optical fiber networks [3,4]. In the recent decade, the number of high-speed terahertz transmission systems has been experimentally demonstrated, with air-interface data rates ranging from 10 to 600 Gbit/s [5–14]. Advanced modulation formats have been employed to improve the system spectral efficiency such as the single-carrier quadrature amplitude modulation (QAM) formats [5,8–10,13] and the multi-carrier orthogonal frequency division multiplexing modulation formats [7,11,12,14]. Comparing the single-carrier with the multi-carrier modulation formats, one can observe that multi-carrier modulation provides higher robustness against terahertz channel impairments, and its channel adaptiveness is better than single-carrier modulation due to its smaller frequency granularity. As a result, up to 600 Gbit/s line rate [14] terahertz communications are demonstrated with multi-carrier modulation.

Although the multi-carrier terahertz communications have shown several benefits, the coherent detection scheme adopted in such systems still hinders their real-world implementation. First, these systems require a coherent heterodyne receiver based on subharmonic radio frequency (RF) mixing with a frequency-multiplied electrical local oscillator (LO), which takes up a major part of the system complexity. Secondly, the signal processing routine at the receiver side is complex, consisting of channel estimation and equalization, I/Q imbalance correction, and phase noise compensation, which in turn may result in power consumption and thermal issues in a packaged module. On the other hand, a simple terahertz direct detection scheme only needs one diode at the receiver to recover the signal envelop of an intensity-modulated terahertz beam [15], providing a cost-effective alternative without additional active RF sources.

In this Letter, we propose and experimentally demonstrate a nonlinearity-aware terahertz discrete multitone (DMT) photonic wireless transmission system operating in the 310 GHz band. In the setup, a cutting-edge uni-traveling-carrier photodiode (UTC-PD) operating in the frequency range of 280–380 GHz (NTT Electronics Corp. IOD-PMJ-13001) is employed as the terahertz emitter, and a zero-bias diode (ZBD) operating in the frequency band 220–330 GHz with a maximum response bandwidth of 40 GHz (Virginia Diode WR3.4ZBD, 1500 V/W) is used to downconvert the terahertz signals to the baseband. Such a DMT-based direct detection

scheme has not yet been applied and studied previously in the terahertz band, to the best of our knowledge.

The system architecture is shown in Fig. 1. In the experiment, the DMT samples are generated offline by MATLAB software and loaded into a 65 GSa/s arbitrary waveform generator (AWG, Keysight M8195A, 3 dB bandwidth: 25 GHz, 8 bit vertical resolution). The inversed fast Fourier transformation (IFFT) point of DMT sample is 2048, of which 480 subcarriers are loaded with 16-ary QAM (16QAM) symbols, and the baseband bandwidth is around 15 GHz. In the terahertz photonic frontend, two tunable external cavity lasers (ECLs) (<100 kHz linewidth) are used as optical sources. The optical carrier from ECL-1 with a wavelength of 1550.01 nm is launched into a polarization controller (PC) to control the polarization state of signal into a Mach–Zehnder modulator (MZM, 25 GHz bandwidth). The DMT samples amplified by a linear amplifier (SHF 807, 24 dB gain) is loaded into the MZM. The baseband optical DMT signal is amplified by an erbium-doped fiber amplifier, filtered by an optical bandpass filter to suppress the out-of-band amplified spontaneous emission noise and polarization aligned with an optical LO (ECL-2, 1552.5 nm) by a PC. A polarizer (Pol.) is used to align the polarization of the signals. The frequency difference between ECL-1 and ECL-2 is 310 GHz. The coupled optical signals are finally sent into an UTC-PD for photo-mixing generation of terahertz signals. The combined optical spectrum of two wavelengths with a 15 GHz DMT signal is shown in Fig. 2. The terahertz signals are then transmitted through a transmitting horn antenna (25 dBi gain) and radiated into a 3 m wireless link with a pair of lenses to collimate the terahertz beam. At the receiver, the terahertz signals are received by a receiving horn antenna (25 dBi gain). A ZBD and a bias-tee are used to recover the baseband DMT signal. The output signal is then amplified by two linear amplifiers (SHF 804, 22 dB gain) and analog-to-digital converted by a real-time digital sampling oscilloscope (DSO, 160 GSa/s, Keysight DSOZ594A, 3 dB bandwidth: 59 GHz) for further digital signal processing (DSP).

The nonlinear impairments are derived as follows.

At the transmitter, a MZM is used to modulate the baseband DMT signal. Assuming that the MZM is biased at its linear region, the electrical field at the output of the MZM is

$$E_1(t) = \sqrt{P_1} \cdot \left\{ a \left[\underbrace{V_{\mathrm{DC}} + \sum_{k=0}^{N-1} X_k e^{j2\pi kt/N}}_{\mathrm{DMT}} \right] + b \right\} \cdot e^{j(\omega_1 t + \varphi_{n1}(t))}, \tag{1}$$

where P_1, ω_1, and φ_{n1} are the power, angular frequency, and phase of an external cavity laser (ECL-1), respectively, and a, b present the modulation depth and intercept of the MZM linear

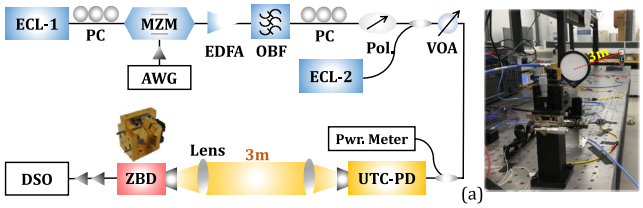

Fig. 1. Experimental setup. (a) Photo of the 3 m wireless link.

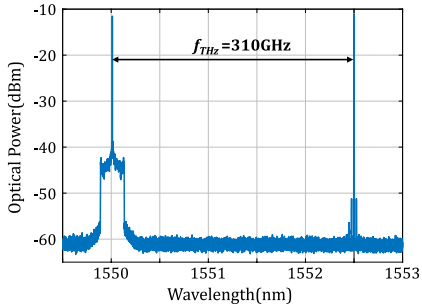

Fig. 2. Optical spectrum before UTC-PD.

region, respectively. V_{DC} is the direct current bias voltage, and N is the number of subcarriers of the DMT symbol.

The optical baseband signal at the frequency of ω_1 is then coupled with another optical carrier with a center frequency of ω_2 from the ECL-2. This laser performs as an optical LO, with an electrical field as $E_2(t) = \sqrt{P_2} \cdot e^{j(\omega_2 t + \varphi_{n2}(t))}$, where P_2, ω_2, and φ_{n2} are the power, angular frequency, and phase, respectively. After the optical combination and photo-mixing at the UTC-PD, the generated terahertz signals is

$$\begin{aligned} E_{\mathrm{THz}}(t) &= [E_1(t) + E_2(t)] \cdot \mathrm{conj}[E_1(t) + E_2(t)] \cdot R_1 \\ &\approx 2R_1\sqrt{P_1 P_2} \cdot \left[a \left(V_{\mathrm{DC}} + \sum_{k=0}^{N-1} X_k e^{j2\pi kt/N} \right) + b \right] \\ &\quad \cdot \cos\left[(\omega_1 - \omega_2)\, t + (\varphi_{n1}(t) - \varphi_{n2}(t)) \right], \end{aligned} \tag{2}$$

where R_1 is the responsivity of the UTC-PD. Subsequently, the terahertz signals are radiated into a wireless link and directly detected by the ZBD, which is a square-law-based component. Considering the output RF bandwidth limitation of the ZBD detector, the output signal can be expressed as Eq. (3):

$$\begin{aligned} E_{\mathrm{ZBD}}(t) &= E_{\mathrm{THz}}(t) \cdot \mathrm{conj}(E_{\mathrm{THz}}(t)) \cdot R_2 \\ &\approx \underbrace{4a\, P_1 P_2 {R_1}^2 R_2 (a\, V_{\mathrm{DC}} + b) \cdot \sum_{k=0}^{N-1} X_k e^{j2\pi kt/N}}_{\mathrm{Received\ DMT}} \\ &\quad + \underbrace{2a^2 P_1 P_2 {R_1}^2 R_2 \left(\sum_{k=0}^{N-1} X_k e^{j2\pi kt/N} \right)^2}_{\mathrm{SSBI}} \\ &\quad + \underbrace{2 P_1 P_2 {R_1}^2 R_2 (a\, V_{\mathrm{DC}} + b)^2}_{\mathrm{DC}}, \end{aligned} \tag{3}$$

where R_2 is the responsivity of the ZBD. To simplify the derivation, here the channel response and impairments in the system are not considered yet. As indicated in Eq. (3), the detected signals contain a desired DMT signal (first-term), a subcarrier-to-subcarrier beating interference (SSBI) component (second-term) and a DC component (third-term). Apparently, the nonlinear distortions caused by SSBI would severely deteriorate the system performance. The electrical spectrum of the received DMT signal is shown in Fig. 3, and the electrical

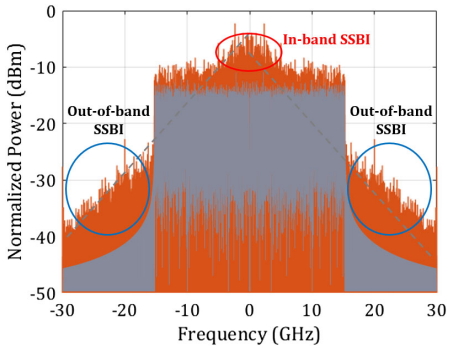

Fig. 3. Electrical spectrum of the received (red color) and transmitted (blue color) DMT signal.

spectrum of the transmitted DMT signal is also inserted for comparison. The SSBI is strong in the received signal; in particular, the in-band SSBI will cause inter-subcarrier-interference-based nonlinear impairments in the receiver of optoelectronic terahertz communication systems.

To estimate the nonlinear impairments and compensate for it in the optoelectronic terahertz multitone communication systems, a nonlinearity-aware DSP routine is employed here. The main part is truncated Volterra nonlinear filtering. In the receiver side offline signal processing, the DMT signal is de-modulated to the frequency domain with traditional FFT operation, a linear equalization (LE) module [16] is first used to estimate the linear channel response and compensate for the linear impairments. At the first iteration, the signal is re-modulated into the time domain to get the estimation of the transmitted temporal samples, which is expressed as $x'(n)$. The Volterra filtering-based nonlinear equalization is expressed as follows:

$$y'(n) = y(n) - \sum_{i=0}^{N_2-1}\sum_{j=i}^{N_2-1} h_2(i,j)x'(n+\alpha-i)x'(n+\alpha-j) - \sum_{i=0}^{N_3-1}\sum_{j=i}^{N_3-1}\sum_{k=j}^{N_3-1} h_3(i,j,k)x'(n+\alpha-i) \times x'(n+\alpha-j)x'(n+\alpha-k), \quad (4)$$

where $y(n)$ is the received DMT samples, $y'(n)$ is the DMT sample after Volterra filtering, and N_i means the memory length of the ith order Volterra kernels. The terms $h_2(i,j)$ and $h_3(i,j,k)$ are the equalization coefficients of 2nd- and 3rd-order Volterra kernels, they are estimated by a recursive least square (RLS) algorithm with the DMT training samples [17,18]. The complexity order of the nonlinear filtering is $O(N_3^3)$. The mean squared error (MSE) versus the DMT training samples is shown in Fig. 4. It can be seen that the MSE is decreasing to a stable value of around −11 dB within one DMT symbol, which corresponds to 2048 DMT samples in Fig. 4. In the experiment, two DMT symbols are used for the training process, and 78 DMT symbols are used for the transmission performance test.

To optimize the transmission performance, the number of memory length and iterations at the receiver side is analyzed, as shown in Figs. 5 and 6. The starting point is the transmission performance with only LE. With the increase of the memory length of the Volterra kernels, more past samples are considered in the Volterra model, and the estimation of the nonlinear

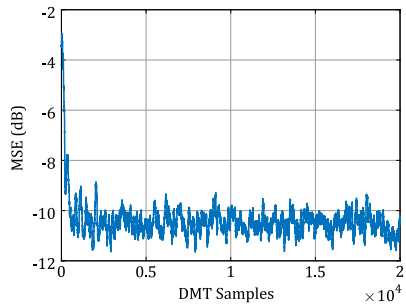

Fig. 4. Convergence curve of RLS-based Volterra filtering.

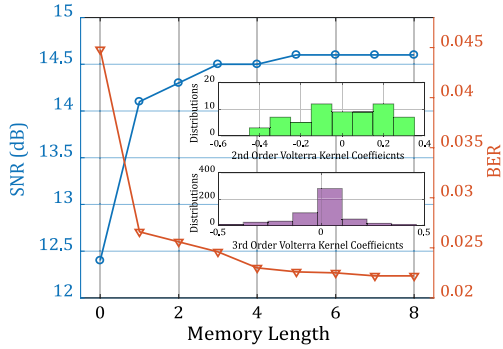

Fig. 5. SNR and BER performance versus the memory length of Volterra filtering. (Inset) Distributions of 2nd- and 3rd-order Volterra kernel coefficients.

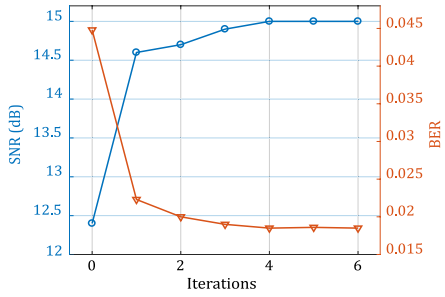

Fig. 6. SNR and BER performance versus the iteration numbers of the Volterra filtering-based receiver.

impairments will be more accurate. The mean signal-to-noise ratio (SNR) is improved with the increment of memory length, and it gets saturated when the memory length is larger than 5, and the bit error ratio (BER) also gets saturated. The theoretical SNR required to obtain the best BER in Fig. 6 is around 14 dB in the additive white Gaussian noise (AWGN) channel, and there is negligible penalty due to residual nonlinearities. In the experiment, the memory length of 6 is used. The distributions of 2nd and 3rd Volterra coefficients are also shown in the inset of Fig. 5, and the 3rd nonlinear distortions are weaker than 2nd nonlinear distortions. Therefore, truncated Volterra nonlinear filtering up to 3rd is enough for the experiment here. Regarding the number of iterations, a similar rule could be observed, and the iteration number of 4 is used here.

The probed SNR versus the subcarrier index is shown in Fig. 7. Without any equalization, the mean SNR is 11.75 dB, and the baseband SNR is deteriorated due to the SSBI effect.

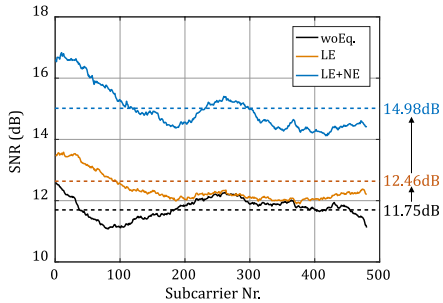

Fig. 7. Probed SNR with a difference signal reception routine.

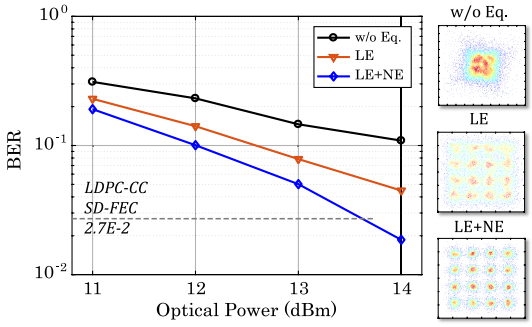

Fig. 8. BER versus the input optical power of the UTC-PD. (Inset) Constellations with a different signal reception routine.

After LE, the mean SNR is improved to 12.46 dB. Then the mean SNR is improved to 14.98 dB after nonlinear equalization (NE), and the SNR is improved by more than 3 dB with the help of LE- and NE-based nonlinearity-aware signal processing routines. The transmission BER performance versus the input optical power of UTC-PD is shown in Fig. 8. Here we use the low-density parity-check convolutional code (LDPC-CC) soft decision forward error correction (SD-FEC) threshold (2.7 E-2, 20%-OH [19]). The BER is lower than the SD-FEC with nonlinearity-aware DSP when the current is larger than 4 mA. The corresponding constellation graphs are also shown in the insets of Fig. 8. The final air-interface line rate is $15\,\text{GHz} \times 4\,\text{bit/s/Hz} = 60\,\text{Gbit/s}$. The net rate after subtracting the training symbol and the FEC overhead is $60\,\text{Gbit/s} \times (78/80)/(1 + 20\%) = 48.75\,\text{Gbit/s}$. Here a better BER and SNR could be obtained in the system by means such as increasing the terahertz power with power amplifiers or decreasing the wireless link distance.

To conclude, by using a simple intensity modulation and direct detection optoelectronic terahertz transmission system based on a ZBD, we experimentally demonstrated DMT transmission of 60 Gbit/s line rate. With nonlinearity-aware DSP, the measured BER is below the threshold of SD-FEC, and the system SNR is improved by 3 dB. The nonlinearity-aware DSP that depends on the end-to-end optimization is also suitable for general-purpose implementation of an optoelectronic terahertz system; the nonlinear impairments such as the modulation nonlinearity of modulator, clipping of the signal, and the nonlinearity from electrical amplifiers, can also be mitigated with the designed DSP [17]. In addition, the simplified nonlinear filtering schemes such as sparse Volterra filtering [20] could also be introduced in our system to decrease the complexity of DSP.

Funding. The Swedish Research Council (VR) Starting Grant (2019-05197); National Key Research and Development Program of China (2018YFB1801500, 2018YFB2201700); National Natural Science Fund Foundation of China (61771424, 61871345); Zhejiang Lab (2020LC0AD01); Natural Science Foundation of Zhejiang Province (LZ18F010001); Fundamental Research Funds for the Central Universities (2020QNA5012).

Acknowledgment. The authors are grateful for the training platform of information and microelectronic engineering from the Polytechnic Institute in Zhejiang University.

Disclosures. The authors declare no conflicts of interest.

REFERENCES

1. M. Tonouchi, Nat. Photonics **1**, 97 (2007).
2. H. J. Song and T. Nagatsuma, IEEE Trans. THz Sci. Technol. **1**, 256 (2011).
3. T. Nagatsuma, G. Ducournau, and C. C. Renaud, Nat. Photonics **10**, 371 (2016).
4. T. Nagatsuma and G. Carpintero, IEICE Trans. Electron. **E98.C**, 1060 (2015).
5. S. Koenig, D. Lopez-Diaz, J. Antes, F. Boes, R. Henneberger, A. Leuther, A. Tessmann, R. Schmogrow, D. Hillerkuss, R. Palmer, T. Zwick, C. Koos, W. Freude, O. Ambacher, J. Leuthold, and I. Kallfass, Nat. Photonics **7**, 977 (2013).
6. X. Yu, Y. Chen, M. Galili, T. Morioka, P. U. Jepsen, and L. K. Oxenløwe, *16th International Conference on Transparent Optical Networks (ICTON)* (2014).
7. H. Shams, T. Shao, M. J. Fice, P. M. Anandarajah, C. C. Renaud, F. V. Dijk, L. P. Barry, and A. J. Seeds, IEEE Photonics J. **7**, 1 (2015).
8. K. Liu, S. Jia, S. Wang, X. Pang, W. Li, S. Zheng, H. Chi, X. Jin, X. Zhang, and X. Yu, IEEE Photonics Technol. Lett. **30**, 1064 (2018).
9. X. Pang, S. Jia, O. Ozolins, X. Yu, H. Hu, L. Marcon, P. Guan, F. Da Ros, S. Popov, G. Jacobsen, M. Galili, T. Morioka, D. Zibar, and L. K. Oxenløwe, *IEEE Photonics Conference* (2016).
10. X. Li, J. Yu, L. Zhao, W. Zhou, K. Wang, M. Kong, G. K. Chang, Y. Zhang, X. Pan, and X. Xin, *Optical Fiber Communications Conference (OFC)* (2019), paper M4F. 4.
11. S. Jia, M. Lo, L. Zhang, O. Ozolins, A. Udalcovs, D. Kong, X. Pang, X. Yu, S. Xiao, S. Popov, J. Chen, G. Carpintero, T. Morioka, H. Hu, and L. K. Oxenlewe, *Optical Fiber Communications Conference (OFC)* (2019), paper Th1C.2.
12. S. Wang, Z. Lu, W. Li, S. Jia, L. Zhang, M. Qiao, X. Pang, N. Idrees, M. Saqlain, X. Gao, X. Cao, C. Lin, Q. Wu, X. Zhang, and X. Yu, APL Photonics **5**, 056105 (2020).
13. X. Yu, S. Jia, H. Hu, M. Galili, T. Morioka, P. U. Jepsen, and L. K. Oxenløwe, APL Photonics **1**, 081301 (2016).
14. S. Jia, L. Zhang, S. Wang, W. Li, M. Qiao, Z. Lu, N. M. Idrees, X. Pang, H. Hu, X. Zhang, L. K. Oxenløwe, and X. Yu, J. Lightwave Technol. (2020).
15. L. Moeller, J. Federici, and K. Su, *URSI General Assembly and Scientific Symposium* (2011).
16. L. Zhang, M. Bi, S. Xiao, L. Liu, and Z. Zhou, Opt. Commun. **364**, 129 (2016).
17. L. Zhang, X. Hong, X. Pang, O. Ozolins, A. Udalcovs, R. Schatz, C. Guo, J. Zhang, F. Nordwall, K. M. Engenhardt, U. Westergren, S. Popov, G. Jacobsen, S. Xiao, W. Hu, and J. Chen, Opt. Lett. **43**, 182 (2018).
18. K. Zhong, X. Zhou, J. Huo, C. Yu, C. Lu, and A. P. T. Lau, J. Lightwave Technol. **36**, 377 (2018).
19. D. Chang, F. Yu, Z. Xiao, N. Stojanovic, F. N. Hauske, Y. Cai, C. Xie, L. Li, X. Xu, and Q. Xiong, *Optical Fiber Communication Conference (OFC)* (2012), paper OW1H.4.
20. C. Chuang, W. Chang, C. Wei, C. Ho, C. Huang, J. Shi, L. Henrickson, Y. Chen, and J. Chen, *Optical Fiber Communication Conference (OFC)* (2019).